



Effect of Cr addition on γ - γ' cobalt-based Co–Mo–Al–Ta class of superalloys: a combined experimental and computational study

B. Nithin¹, A. Samanta², S. K. Makineni^{1,4,*}, T. Alam³, P. Pandey¹, Abhishek K. Singh², R. Banerjee³, and K. Chattopadhyay¹

¹Department of Materials Engineering, Indian Institute of Science, Bangalore 560012, India

²Materials Research Centre, Indian Institute of Science, Bangalore 560012, India

³Center for Advanced Research and Technology, Department of Materials Science and Engineering, University of North Texas, Denton, TX, USA

⁴Present address: Department of Microstructure Physics and Alloy Design, Max-Planck-Institut für Eisenforschung GmbH, 40237 Düsseldorf, Germany

Received: 19 November 2016

Accepted: 29 April 2017

Published online:

12 June 2017

© The Author(s) 2017. This article is an open access publication

ABSTRACT

The present article deals with effect of Cr addition (10 at.%) on the partitioning behavior and the consequent effect on mechanical properties for tungsten-free γ - γ' cobalt-based superalloys with base alloy compositions of Co–30Ni–10Al–5Mo–2Ta (2Ta) and Co–30Ni–10Al–5Mo–2Ta–2Ti (2Ta2Ti). Cr addition leads to a change in the morphology of the strengthening cuboidal-shaped γ' precipitates to a spherical shape. The site preference of Cr atoms in two alloy systems (with and without Ti) has been experimentally investigated using atom probe tomography with the supportive prediction from first principles DFT-based computations. Cr partitions more to the γ matrix relative to γ' . However, Cr also has a strong effect on the Ta and Mo partitioning coefficient across γ/γ' interfaces. The value of partition coefficient for Mo (K_{Mo}) becomes <1 with Cr addition to the alloys. Results from ab initio calculations show that the Cr atoms prefer to replace Mo atoms in the sublattice sites of the $L1_2$ unit cell. The solvus temperature of about 1038 and 1078 °C was measured for 10Cr2Ta and 10Cr2Ta2Ti alloy, respectively, and these Cr-containing alloys have very low densities in the range of ~ 8.4 – 8.5 gm/cm^{−3}. The 0.2% compressive proof strength of 10Cr2Ta2Ti alloy yields a value of 720 MPa at 870 °C, substantially better than most Co–Al–W-based alloys and many of the nickel-based superalloys (e.g., MAR-M-247).

Address correspondence to E-mail: surendra.makineni@gmail.com

Introduction

Production of materials capable of sustaining high temperatures with high strength and hot corrosion resistance will remain a key attraction and challenge for material scientists. These materials are required for fabricating critical parts in hot section of turbine engines (both aero and land based) where the temperature touches 1600 °C [1–3]. The cobalt-based alloys have often been considered as a possible alternative to nickel-based superalloys that are commercially successful in both polycrystalline and single-crystal form. Generally, these alloys were strengthened through solid solution strengthening and contain metal carbides [4, 5]. Efforts toward the use of cobalt-based alloys have accelerated in recent time when γ - γ' microstructure in the Co–Al–W was exploited in developing newer alloys [6–9]. Cobalt-based superalloys were known for their excellent oxidation and hot corrosion resistance at high temperatures compared to nickel-based superalloys [10–12]. But due to their low strength values, these were unable to compete with nickel-based superalloys that are being used with expensive thermal barrier coatings [13, 14]. Significant increase in resistance to oxidation at high temperatures is reported by addition of Cr to γ - γ' Co–Al–W-based alloys by several research groups and found to be better than even nickel-based superalloys [15–17]. To further advance the high-temperature creep properties, alloying additions such as B, Ta, Ti were carried out that yielded better properties [18–23]. The γ' precipitate-coarsening kinetics in Co–Al–W has been also established [24, 25].

Recently, addition of Ni to these cobalt-based superalloys has shown to increase the limit of refractory element content as otherwise these are more susceptible to decomposition and unwanted TCP phase formation at high temperatures [26–29]. This is mainly due to narrow γ' phase stability of Co–Al–W system, and thus, Ni increases the γ' phase field and also increases the solvus temperature of the alloy. In addition, these alloys exhibit better mechanical, creep and oxidation properties [30, 31]. But the densities of these alloys have been always at the higher range (>9.5 gm.cm⁻³) due to high W content that is a necessary constituent for obtaining γ - γ' microstructure. Although several attempts were made [32, 33], reduction of W remains a challenge.

Recent reports on new γ - γ' cobalt superalloys based on Co–Al–Mo–Nb/Ta system that does not contain W have opened up new possibilities in designing high-temperature alloys with lower densities [34–36]. The γ - γ' microstructure is stabilized in these alloys by a small addition of Nb or Ta. The solvus temperature as well as the stability of γ' can be further increased by the addition of Ni (up to 30 at.%) and Ti (2at.%) to the base alloy (Co–10Al–5Mo–2Ta/Nb) [37]. Thus, new Co–Ni-based superalloys with densities in the range of 8.2–8.6 gm.cm⁻³ (comparable to nickel-based superalloys) and solvus temperature of greater than 1050 °C with an attractive 0.2% proof strength at temperatures ~ 800 °C and above are possible. It has been also shown recently that the creep properties of these alloys are comparable to Co–Al–W-based alloys [38, 39].

Chromium is integral to the modern superalloys as it imparts good environmental and mechanical properties [40, 41]. Recently, it was also found that Cr influences the morphology of γ' precipitates by effecting the partitioning of W across γ/γ' interface in Co(Ni)–Al–W-based alloys that reduces the lattice misfit [42]. The Cr effect in the new tungsten-free alloys is yet to be explored. The present work deals with the chromium influence on the two base alloys Co–30Ni–10Al–5Mo–2Ta and Co–30Ni–10Al–5Mo–2Ta–2Ti having solvus temperatures >1030 °C [36]. The partitioning behaviors of the alloying elements in the γ and γ' phases in the presence of Cr that were obtained through APT experiments were compared with the results of first principle calculations. To assess the suitability of these alloys for structural application, the preliminary mechanical properties of these chromium-added superalloys were also evaluated.

Materials and methods

Arc melting

A laboratory-scale vacuum arc melting unit was used to melt alloys of nominal compositions (as shown in Table 1) under argon atmosphere in the form of 30 grams ingots in a water-cooled copper hearth.

The alloys were melted 10–12 times to obtain homogenized alloy composition throughout the

Table 1 Nominal and measured composition (at.%) of the alloys

Alloy designation	Alloys	Measured composition
10Cr2Ta	Co–30Ni–10Cr–10Al–5Mo–2Ta	Co–31.2 ± 0.3Ni–10.5 ± 0.6Cr–10.1 ± 0.3Al–5.1 ± 0.3Mo–2.1 ± 0.3Ta
10Cr2Ta2Ti	Co–30Ni–10Cr–10Al–5Mo–2Ta–Ti	Co–30.4 ± 0.6Ni–11.5 ± 0.7Cr–9.7 ± 0.2Al–5.2 ± 0.3Mo–2.2 ± 0.2Ta–2.1 ± 0.2Ti

ingot. Subsequently, these were cast into 3-mm rods using a vacuum arc suction casting unit equipped with a water-cooled split copper mold. The composition of the alloys was measured by using WDS detector in a field emission tipped EPMA (JEOL).

Heat treatment

The rods were further solutionized at 1300 °C for 15 h under vacuum (10^{-5} bar) followed by quenching in cold water. Samples were cut from the solutionized rods and were sealed in vacuum quartz tubes for aging treatment. Aging was carried out at 900 °C for 50 h in a box furnace and subsequently furnace cooled.

TEM and APT measurements

For the preparation of TEM samples, 3-mm disks from the heat treated samples were cut and mechanically polished to a thickness of ~80 microns. The final samples were prepared by using a twin jet electropolishing unit with a solution of methanol and 5 vol% perchloric acid at –30 °C. A transmission electron microscope (F30, FEI make) equipped with field emission gun and operating at 300 kV was used for microstructural investigation. Accurate measurements of the elemental partitioning across the interface, atom probe tomography (APT) of the aged samples were carried out. The samples for APT investigation were prepared by using a dual-beam focused ion beam instrument (FIB) (FEI NOVA 200). The APT experiments were carried out using a local electrode atom probe (LEAPTM 3000X HR) system in the laser evaporation mode at a temperature of 40 K, with an evaporation rate of 0.5–0.7%, pulse energy of 0.5 nJ and a pulse frequency of 160 kHz. Data analysis was performed using IVASTM 3.6.8 software.

DSC, density and compression tests

Differential scanning calorimetry (DSC) was used to determine the solvus temperature of the aged samples under an argon atmosphere with a heating rate of 10 °C/min. Compression tests to evaluate the 0.2% proof stress of the alloys were performed using a DARTEC hydraulic machine operated with a strain rate of 10^{-3} s⁻¹. The density of the alloys were measured in accordance with the ASTM standard B311-08 at room temperature, while the volume fraction of γ' precipitates for the aged alloys were measured using ASTM standard E562-11.

Ab initio calculations

Methodology for ab initio calculations The total energy and electronic structures of all the crystal structure were calculated using projector augmented wave method based on spin-polarized density functional theory (DFT). The electron and ion interaction is represented by all-electron projector augmented wave potentials as implemented in the Vienna ab initio simulation package (VASP) [43–45]. The exchange and correlation potential of electrons is represented by Perdew–Burke–Ernzerhof functional form within generalized gradient approximation (GGA) [46]. We have used pseudo-potential with valence configurations $3d^7 4s^2$, $3d^8 4s^2$, $3s^2 3p^1$, $4d^5 5s^1$, $3d^5 4s^1$, $3s^2 3p^6 4s^2 3d^2$ and $6s^2 5d^3$, Co, Ni, Al, Mo, Cr, Ti and Ta, respectively. We have considered 48 atoms of $2 \times 2 \times 3$ supercell for our study. Before final SCF calculation, the lattice parameters, as well as the ionic position of ions of each crystal structure, are optimized. The crystal structure was optimized using the conjugate gradient scheme until the forces and total energy are less than $\leq 10^{-3}$ and $< 10^{-4}$ eV/Å, respectively. The electronic wave functions were represented by plane wave basis set with the cutoff

energy of 300 eV. Brillouin zone was sampled by $5 \times 5 \times 3$ Monkhorst–Pack (MP) [47] k -mesh with a smearing width of 0.2 eV. These combinations of k points, smearing width and energy cutoff are provided a good convergence total energy. The formation energy (ΔH^f) of compound is calculated using the following formula [48]

$$\Delta H^f = E_{\text{total}}^{\text{pristine}} - \sum_j n_j \mu_j \tag{1}$$

$E_{\text{total}}^{\text{pristine}}$, n_j and μ_j , which are the total energy of the supercell, number of atom of i th species in the supercell and chemical potential of the i th species, respectively. The defect/impurity formation energy is calculated by [48]

$$\Delta E^f = E_{\text{total}}^{\text{defected}} - E_{\text{total}}^{\text{pristine}} - \sum_j n_j \mu_j \tag{2}$$

where, $E_{\text{total}}^{\text{pristine}}$, $E_{\text{total}}^{\text{defected}}$, n_j and μ_j are the total energy of the supercell, the total energy of the defected cell, number of atom of i th species in the supercell and chemical potential of the i th species, respectively. The chemical potential μ_j of i th species is considered the total energy per atom of their most stable phase. Here, the hexagonal close-packed (hcp) structure for Co, face-centered cubic (fcc) structure for Al and Ni and body-centered cubic (bcc) structure for Mo, Ta and Cr are considered as their most stable states. The lattice parameters for a given composition are considered same for all the configurations.

Results and discussion

Microstructural analysis

Figure 1a, b shows SEM micrograph using secondary electron mode of Co–30Ni–10Cr–10Al–5Mo–2Ta (10Cr2Ta) and Co–30Ni–10Cr–10Al–5Mo–2Ta–2Ti (10Cr2Ta2Ti) alloys after aging at 900 °C for 50 h. In both the alloys, we observe spherical precipitates with relatively higher volume fraction for Ti-containing alloy. The diffraction patterns along [001] zone axis contain superlattice reflections along with the main fcc reflections for both the alloys. These superlattice reflections correspond to $L1_2$ ordering in fcc matrix. Micrographs obtained using STEM HAADF detector (Z-contrast images) were also shown (Fig. 1c, d). These were also taken near [001]

zone axis of the fcc matrix. For 10Cr2Ta alloy, the diameter of the ordered γ' precipitates was in the range of 250–300 nm and has a volume fraction of around 64%. Addition of 2 at.% Ti increases the volume fraction to around 71% with sizes similar to that of original alloy. In the Ti-containing alloy, some of the precipitates were found to be interconnected/coagulated and have smaller inter-particle distance. The spherical morphology of the precipitates in both the alloys can be attributed to the lower lattice misfit between the γ matrix and γ' precipitates that cause lowering of the interfacial energy. If the misfit deviates toward positive or negative, the precipitates take up the cuboidal shape [49]. The lattice misfit at the interface depends on the relative chemistry across the interface and atomic sizes of the constituent elements in both γ matrix and γ' precipitate. The alloys that do not contain Cr exhibits $L1_2$ ordered precipitates with cuboidal morphology [34]. Hence, with the variation of Cr content in these alloys, the lattice misfit at the γ/γ' interface can be modulated or controlled. This can play an important role in the coarsening behavior of the γ' precipitates at high temperatures.

Figure 2 shows APT reconstructions with the γ/γ' interface for both 10Cr2Ta and 10Cr2Ta2Ti alloys. The green and red atoms belong to Ta and Mo, respectively. Table 2 shows the compositions of γ matrix, γ' precipitate and the calculated partitioning coefficients of the respective constituent elements for both the aged alloys. For comparison of the values with the alloys that do not contain Cr, the compositions of γ and γ' for Co–30Ni–10Al–5Mo–2Ta (2Ta) and Co–30Ni–10Al–5Mo–2Ta–2Ti (2Ta2Ti) alloys taken from the Ref. [34] were also included. The partitioning coefficient (K) is calculated by the formula $K = C_{\gamma'}/C_{\gamma}$ (where $C_{\gamma'}$ and C_{γ} are concentration of the element in the ordered γ' precipitate and matrix γ phase, respectively).

From the measured compositions, it is clear that Cr partitions to γ matrix with respect to the γ' precipitates with similar partitioning coefficient (K_{Cr}) of 0.26 and 0.24 in 10Cr2Ta and 10Cr2Ti2Ti alloys while Al and Ta partition to γ' precipitates with the respect to γ matrix with partitioning coefficients $K_{\text{Al}} > 2$ and $K_{\text{Ta}} > 9$, respectively, in both the alloys. In addition, the Ta partitioning in γ' with respect to γ is measured to be more in Cr-containing alloys compared to 2Ta and 2Ta2Ti alloys [34]. Similarly in 10Cr2Ta2Ti, Ti strongly partitions to the γ' precipitate with $K_{\text{Ti}} > 6$,

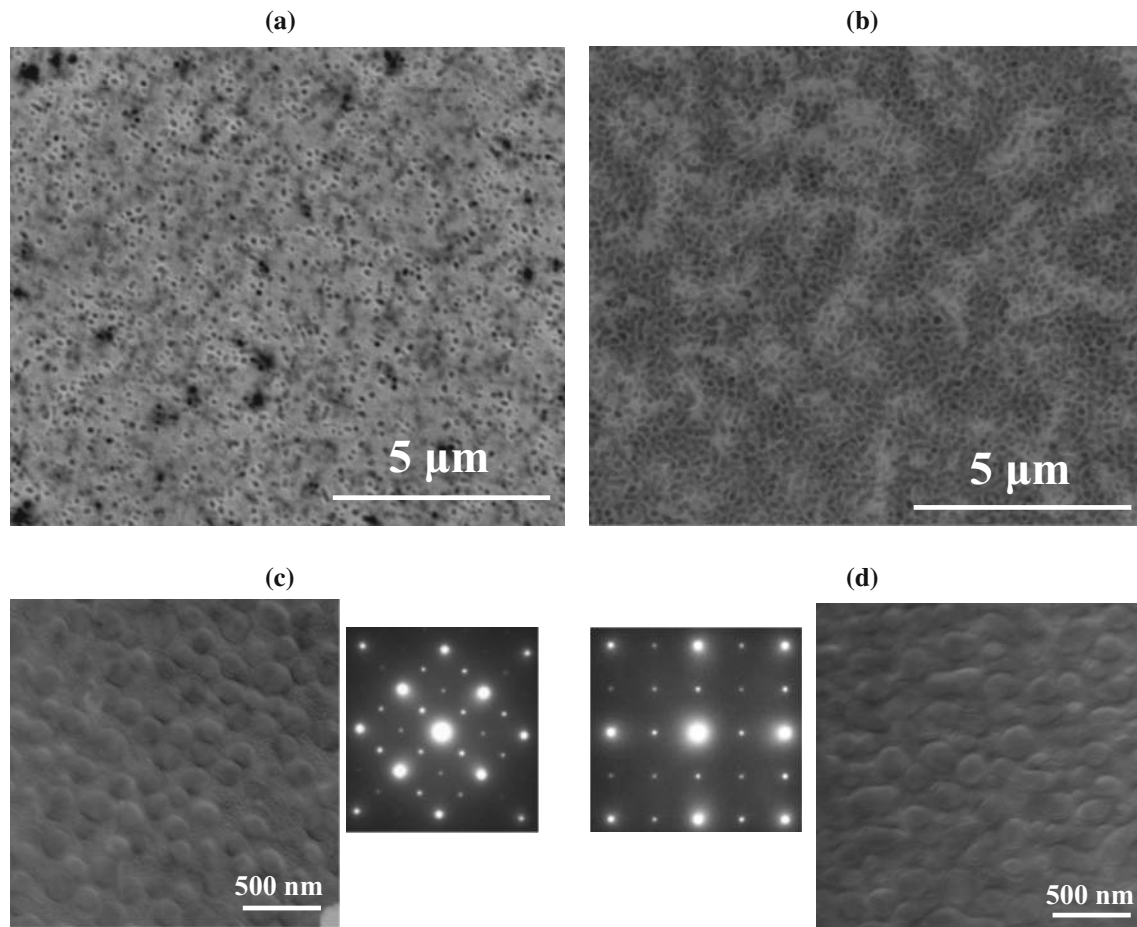


Figure 1 Secondary electron micrograph for **a** Co–30Ni–10Cr–10Al–5Mo–2Ta (10Cr2Ta) and **b** Co–30Ni–10Cr–10Al–5Mo–2Ta–2Ti (10Cr2Ta2Ti) alloys aged for 50 h at 900 °C. Diffraction

patterns taken along [001] zone axis and STEM HAADF contrast images near to [001] zone axis for **c** 10Cr2Ta and **d** 10Cr2Ta2Ti.

and since Co_3Ti with $L1_2$ crystal structure is a stable phase in binary Co–Ti phase diagram, it can be deduced that Ti will occupy the $\{0, 0, 0\}$ sublattice positions of the $L1_2$ unit cell along with Al, Mo and Ta.

On the other hand, the partitioning coefficient for Mo (K_{Mo}) in both the alloys turns out to be <1 due to the addition of Cr. The K_{Mo} values for both the alloys are measured to be similar. The alloys (2Ta and 2Ta2Ti) that do not contain Cr show $K_{\text{Mo}} > 1$ suggesting that the Cr atoms prefer to replace Mo atoms in the $L1_2$ unit cell and occupy those sites. In Co(Ni)–Al–W–based alloys [42], Cr strongly reduces the partitioning of W in γ' with respect to γ and occupies $\{0, 0, 0\}$ sites. This leads to reduction in the γ' lattice parameter and hence reduces the lattice misfit across γ/γ' interface. This is due to substitution of larger size W atoms (139 pm) by smaller Cr atoms (128 pm). Similarly, it can be proposed, in the present case, that the larger size Mo atoms (139 pm) are replaced by smaller Cr atoms in the γ' $L1_2$ unit cell that reduces its

lattice parameter while the γ matrix lattice parameter raises due to increase in Mo content in the γ matrix. Even though there is increase in the Ta (146 pm) partitioning in γ' after Cr addition, the overall effect on misfit reduction is more prominent due to reversal of Mo partitioning across γ/γ' and hence results in morphological transition of the γ' precipitates from cuboidal to spherical. In Co(Ni)–Al–W–Cr–Mo–based alloys [50], it was also observed that Mo partitions relatively higher in γ matrix with respect to γ' precipitate. However, no suitable explanation for the reversal is presented. Figure 2 shows comparison of Mo concentration variation across the γ/γ' interface for 2Ta/2Ta2Ti and 10Cr2Ta/10Cr2Ta2Ti alloys. It can be seen further significant level of Mo segregation at the γ/γ' interface in 2Ta/2Ta2Ti (without Cr) alloys compared to 10Cr2Ta/10Cr2Ta2Ti alloys. Segregation of different elements at γ/γ' interface has also been reported in Ni-based superalloys that contribute to reduction in interfacial energy [51, 52]. For

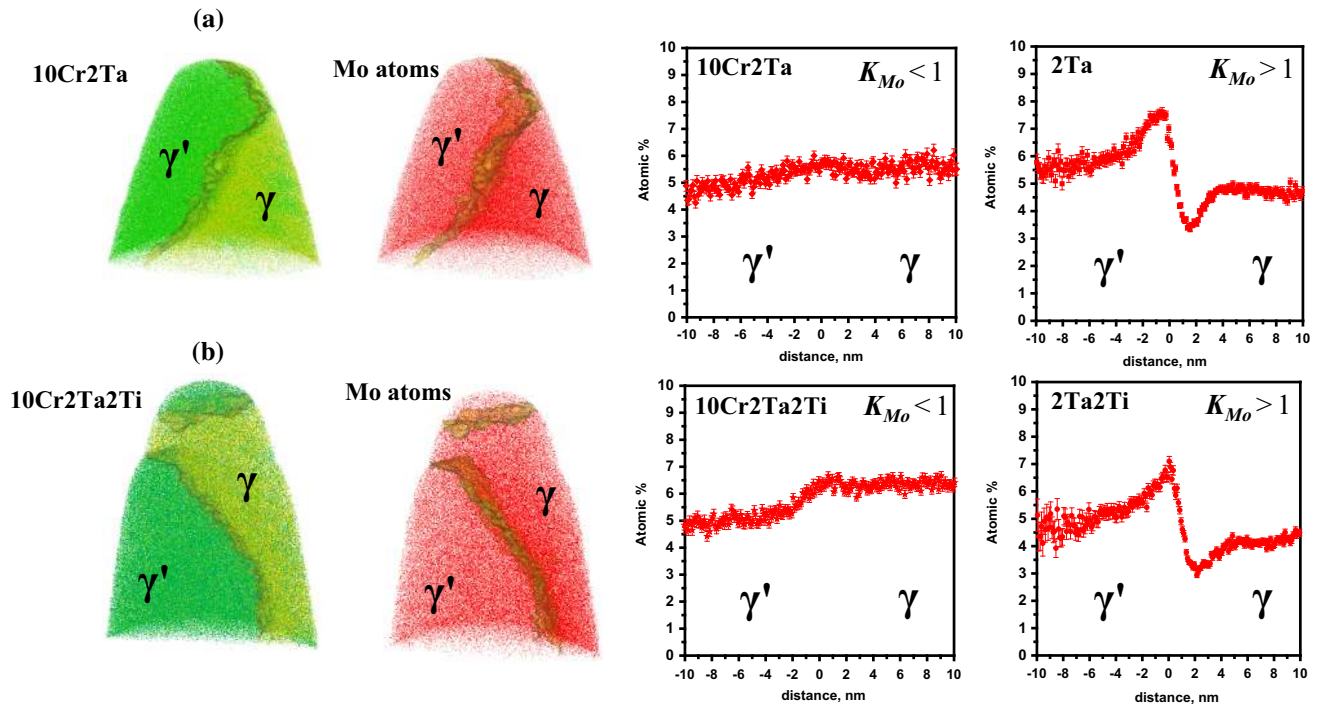


Figure 2 APT reconstruction showing the γ/γ' (Ta atoms—green, Mo atoms—red) interface and comparison of variation of Mo concentration across the interface for both **a** Co–30Ni–10Cr–10Al–5Mo–2Ta (10Cr2Ta) alloy and **b** Co–30Ni–10Cr–10Al–5Mo–2Ta–2Ti (10Cr2Ta2Ti) alloy with alloys that do not contain Cr (2Ta and 2Ta2Ti).

Table 2 Composition of γ and γ' for 10Cr2Ta and 10Cr2Ta2Ti alloys and their comparison with alloys that do not contain Cr

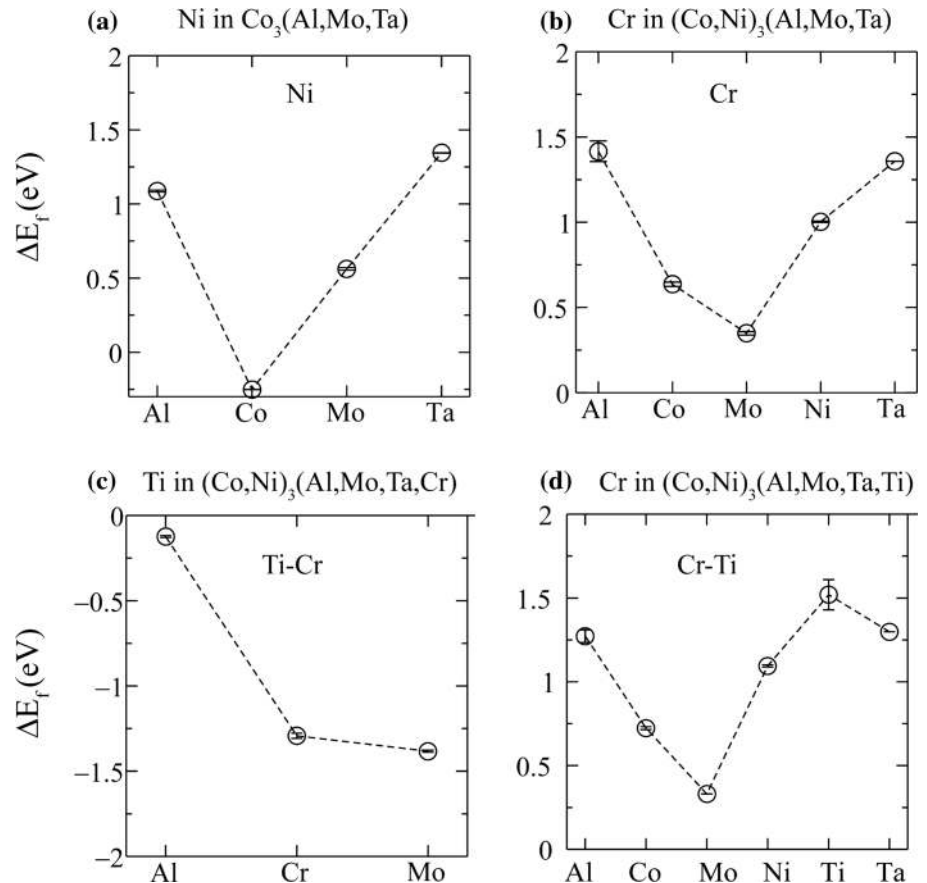
10Cr2Ta			10Cr2Ta2Ti			2Ta [34]			2Ta2Ti [34]			
Co–30Ni–10Cr–10Al–5Mo–2Ta			Co–30Ni–10Cr–10Al–5Mo–2Ta–2Ti			Co–30Ni–10Al–5Mo–2Ta			Co–30Ni–10Al–5Mo–2Ta–2Ti			
γ_p	γ'_p	K_i	γ_p	γ'_p	K_i	γ_p	γ'_p	K_i	γ_p	γ'_p	K_i	
Co	50.98	34.45	0.68	49.75	36.71	0.74	62.84	34.93	0.56	62.78	33.26	0.53
Ni	21.12	38.35	1.82	18.35	35.67	1.94	26.34	41.83	1.59	26.23	43.16	1.65
Al	5.43	14.98	2.76	5.54	12.72	2.30	5.61	14.94	2.66	5.8	15.22	2.62
Mo	5.62	4.87	0.87	6.36	4.98	0.78	4.72	5.72	1.21	4.17	4.99	1.2
Ta	0.21	2.95	14.05	0.27	2.69	9.96	0.47	2.55	5.43	0.35	1.89	5.4
Ti	–	–	0.39	0.39	2.61	6.69	–	–	–	0.65	1.45	2.23
Cr	16.61	4.4	0.26	19.32	4.62	0.24	–	–	–	–	–	–

example, in Ni–Al–Cr–W alloy, the γ/γ' interface exhibits a preferential W segregation in flat 100 type facets with respect to other hkl planes (non-100 planes—curved interfaces). This is due to relatively higher reduction in interfacial free energy by W segregation on 100 facets that stabilizes the cuboidal morphology [53]. Similarly, in the present case, we observe Mo segregation on flat γ/γ' interfaces (100 type facets), while there was no evidence of interfacial Mo segregation in curved interfaces (spherical precipitates in Cr-containing alloys). Hence, it is

likely that in addition to the reason of higher misfit across γ/γ' interface for cuboidal morphology, the Mo segregation at the interface is also an important contributing factor for faceted γ' precipitates in γ matrix.

An additional and critical observation is that the measured percentage of total content of Co + Ni in γ' phase is <73% for the both Cr-containing alloys while the values for the alloy that does not contain Cr (2Ta and 2Ta2Ti) are >76%. This indicates that Cr atoms will also prefer to occupy partially the {1/2, 1/2, 0}

Figure 3 Impurity formation energy for **a** Ni substitute in $\text{Co}_3(\text{Al,Mo,Ta})$, **b** Cr in $(\text{Co,Ni})_3(\text{Al,Mo,Ta})$, **c** Ti in $(\text{Co,Ni})_3(\text{Al,Mo,Ta,Cr})$, **d** Cr in $(\text{Co,Ni})_3(\text{Al,Mo,Ta,Ti})$.



lattice sites (along with Co and Ni). It can be noted that the site substitution preference of Cr in nickel-based superalloys is also found to be dependent on alloy composition and aging conditions. For example, Booth-Morrison et al. [54, 55] showed that Cr and Al atoms will occupy $\{0, 0, 0\}$ sublattice positions in $L1_2$ unit cell in the case of Ni–Al–Cr alloy. However, the addition of strong γ' stabilizers, such as Ta, favors replacing Cr from these sublattice sites and occupy them. They have shown through ab initio calculations that the difference in substitutional energies for Cr in Ni and Al sites is very small and hence Cr has a very weak preference for $\{0, 0, 0\}$ sublattice positions.

Ab initio calculations

Ab initio calculations were carried out to know the site preference of Cr atoms in the $L1_2$ unit cell and compare the results with the experimental findings.

The basic stoichiometry of $\text{Co}_3(\text{Al,Mo,Ta})$ with the composition (37Co–6Al–3Mo–2Ta—48 atom unit cell) close to experimental value [36] was chosen as the base intermetallic compound in the $L1_2$ structure for the first principle calculations. The substitute element will be thermodynamically unfavorable at a site if the impurity formation energy is greater than 1 eV/atom. First, the site preference of Ni in the base unit cell was checked. The calculated impurity formation energy of Ni at different site occupancy is shown in Fig. 3a. The impurity formation energy of Ni in Co site is lowest among the other sites that indicate Ni will strongly prefer to occupy $\{1/2, 1/2, 0\}$ lattice sites along with Co atoms.

Following this, the site preference of Cr was calculated in the stoichiometry $(\text{Co,Ni})_3(\text{Al,Mo,Ta})$ with the following number of atoms Co–20Ni–7Al–3Mo–1Ta (48-atom unit cell) that is close to the measured composition from Ref. [36]. To calculate impurity

formation energy for Cr substitution in Ta sites, we have considered 96-atom unit cell by keeping composition same as 48-atom unit cell. The calculated impurity formation energy is shown in Fig. 3b, and it indicates that the Cr will prefer to replace Mo atoms present in the $\{0, 0, 0\}$ sublattice sites and occupy them. This is consistent with the experimentally observed change in partitioning coefficient of Mo ($K_{Mo} < 1$ from $K_{Mo} > 1$) after the addition of Cr to the alloy.

Similarly, to know the effect of Ti addition (a strong γ' stabilizer), a unit cell of the stoichiometry $(Co,Ni)_3(Al,Mo,Ta,Cr)$ having the number of atoms $Co-20Ni-7Al-2Mo-2Cr-1Ta$ (48-atom unit cell) with the composition close to the experimental value obtained for the precipitate in containing $10Cr2Ta2Ti$ was assumed. The impurity formation energy for Ti in the unit cell at different positions is shown in Fig. 3c. Ti exhibits similar tendency or preference to replace Mo or Cr present in the $\{0, 0, 0\}$ sublattice positions. In addition, it is observed experimentally that there is no change in the partitioning coefficient of Mo (K_{Mo}) after the addition of Ti. This shows Ti will tend to replace Cr atoms from the $\{0, 0, 0\}$ sublattice positions and hence Cr has a weak preference for these sites when a strong γ' stabilizer is introduced into the unit cell.

The site substitution behavior of Cr into the unit cell $(Co,Ni)_3(Al,Mo,Ta,Ti)$ is also calculated, and Fig. 3d shows the impurity formation energy for Cr atom at different lattice positions of the unit cell

having number of atoms $Co-20Ni-7Al-2Mo-2Ti-1Ta$ (in calculation of impurity formation energy for Cr substitution in Ta sites, we have considered 96-atom unit cell by keeping composition same as 48-atom unit cell). Even in the presence Ti, the Cr prefers to replace Mo atoms present in $\{0, 0, 0\}$ sublattice sites compared to other atoms.

Solvus and density

Figure 4a shows the comparison of solvus temperatures of $10Cr2Ta/10Cr2Ta2Ti$ alloys with $2Ta/2Ta2Ti$ alloys, $Co-9Al-9.8W$ alloy and nickel-based Waspaloy [56]. $10Cr2Ta$ alloy has a solvus temperature value of $1038^\circ C$, while $10Cr2Ta2Ti$ alloy has $1078^\circ C$ that are higher than $2Ta$ ($1014^\circ C$) and $2Ta2Ti$ ($1066^\circ C$), respectively. The solvus temperature is the dissolution temperature of γ' precipitates in γ matrix that depends on stability of the precipitates. The higher values for Cr-containing alloys can be attributed to increase in Ta partitioning in γ' precipitate with respect to γ matrix (Table 2) since Ta acts as a strong γ' stabilizer. The solvus values are even higher than $Co-9Al-9.8W$ ($990^\circ C$) and nickel-based Waspaloy ($1030^\circ C$). In nickel-based superalloys, Cr addition usually acts as γ' solvus suppresser [41, 57]. The densities of $10Cr2Ta$ and $10Cr2Ta2Ti$ were measured to be 8.51 and 8.41 $gm.cm^{-3}$, respectively, that are much lower than existing cobalt-based superalloys and are comparable to nickel-based superalloys (Fig. 4b).

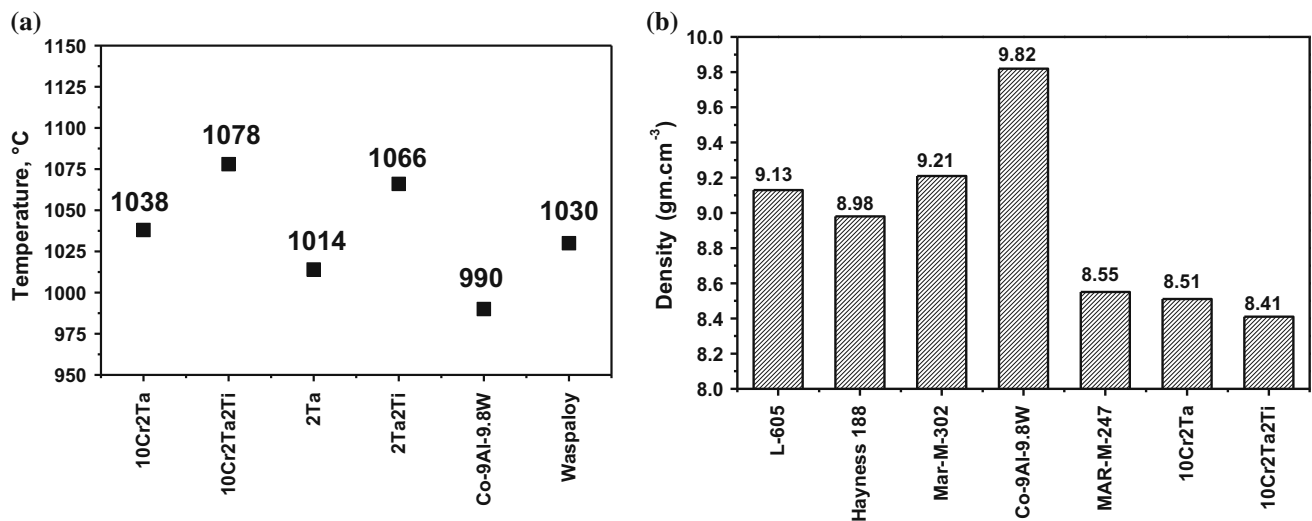


Figure 4 Comparison of **a** solvus temperatures and **b** densities of present Cr-containing alloys with commercially available cobalt-based and nickel-based superalloys.

Mechanical properties

As the addition of Cr significantly influences the coherency of the γ/γ' interface, this is expected to influence the mechanical properties. To obtain a preliminary evaluation of the mechanical properties, compression tests were performed on both the alloys. Figure 5a shows a plot of 0.2% proof stress versus temperature for 10Cr2Ta/10Cr2Ta2Ti alloys and compared with 2Ta/2Ta2Ti alloys, commercially available nickel (MAR-M-247) [58] and cobalt-based alloys including Co–Al–W-based alloys [20]. At room temperature 10Cr2Ta and 10Cr2Ta2Ti show 0.2% proof stress of 670 and 720 MPa, respectively, compared to 800 MPa for 2Ta and 740 MPa for 2Ta2Ti alloys. From Ref. [36], the microstructural difference between 2Ta and 2Ta2Ti alloys is the presence of significant volume fraction of secondary precipitates (size <20 nm) in γ matrix channel for 2Ta alloy compared to 2Ta2Ti alloy. Thus, the higher value of 0.2% proof stress for 2Ta alloy can be attributed to possible additional strengthening contribution from weak pair coupling of dislocations during their interaction with these small secondary precipitates. This contribution increases up to a critical precipitate size above which strong pair coupling mechanism takes over that reduces the strengthening with the increasing precipitate size. Very low volume fraction of secondary precipitates in 2Ta2Ti alloy can be attributed to steeper solvus curve at 900 °C (aging temperature) due to increment in solvus temperature by 52 °C. This also supports a significant rise in primary γ' volume

fraction to 74 from 56% after Ti addition. Now, from the study of microstructures after addition of Cr to 2Ta and 2Ta2Ti alloy, we could observe that the volume fraction of primary γ' precipitates increases significantly for 10Cr2Ta alloy ($\sim 64\%$) and remains similar for 10Cr2Ta2Ti alloy ($\sim 71\%$). Hence, the solute supersaturation in the matrix at 900 °C reduces that led to reduction in fraction of secondary γ' precipitates formed during cooling in 10Cr2Ta alloy which explains relatively higher reduction in 0.2% proof stress values due to decreasing contribution from weak pair coupling mechanism. The reduction in 0.2% proof stress after Cr addition also has contribution from the reduced strain associated with the misfit at the γ/γ' interface. Even though the temperature-dependent 0.2% proof stress remains similar till 670 °C for both the alloys, they show a significant increase at 870 °C followed by a reduction. This type of stress anomaly at high temperature was not significant in 2Ta and 2Ta2Ti alloys. However, it was also shown to exist mildly in Co–9Al–9.8W and more prominently in Ta-containing Co–8.8Al–9.8W–2Ta alloys (Fig. 5a) [20, 59] and some of the nickel-based superalloys containing L_{12} ordered precipitates in the fcc matrix [60, 61]. This is generally due to the activation of multiple slip modes at high temperatures within ordered γ' precipitates, i.e., pinning of cross-slipped $1/2\langle 110 \rangle$ superpartial dislocations from the $\{111\}$ octahedral planes to $\{100\}$ cube planes that are driven by elastic anisotropy or lower APB energy on $\{100\}$ planes. In Co–8.8Al–9.8W–2Ta alloy, an extended anomalous strengthening was observed compared to

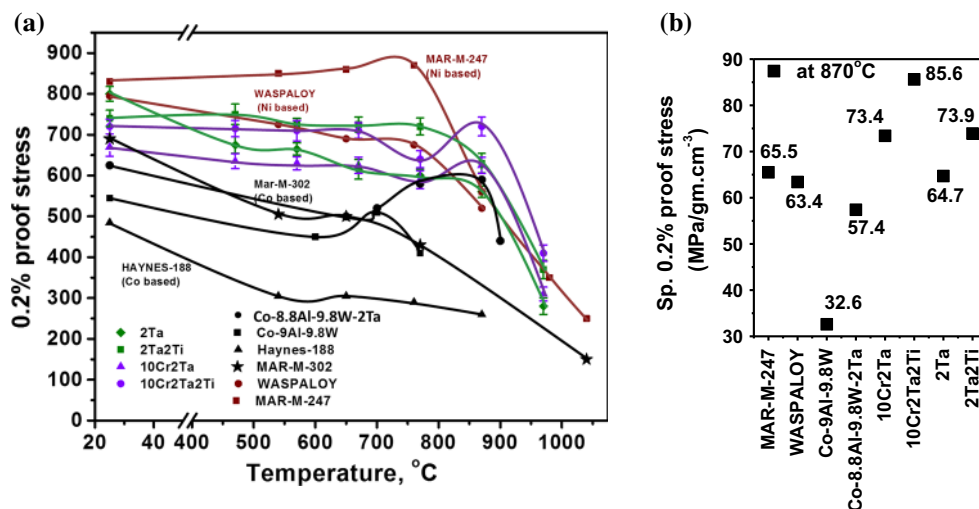


Figure 5 a Plot of 0.2% proof stress versus temperature and b specific 0.2% proof stress at 870 °C of Co–30Ni–10Cr–10Al–5Mo–2Ta (10Cr2Ta) and Co–30Ni–10Cr–10Al–5Mo–2Ta–2Ti (10Cr2Ta2Ti) alloys with other cobalt-based and nickel-based superalloys.

ternary Co–9Al–9.8W alloy. This was attributed to increased stacking fault energy of γ' precipitates due to the presence of Ta in the L₁₂ phase that requires higher shear stress for dislocation to initiate the penetration across the γ' precipitate [62]. The relatively pronounced stress anomaly behavior in 10Cr2Ta and 10Cr2Ta2Ti can be due to significant increase in Ta partitioning to γ' precipitates with respect to γ matrix that is responsible for increasing the stacking fault energy of L₁₂ γ' phase. The 10Cr2Ta and 10Cr2Ta2Ti alloys exhibit 0.2% proof stress value of 625 and 720 MPa at 870 °C, much higher than that observed for 2Ta/2Ta2Ti alloys, Co–8.8Al–9.8W–2Ta alloy (590 MPa) and MAR-M-247 nickel-based superalloys (560 MPa). In Co–Al–W-based superalloys, Cr addition does not contribute to strengthening of the alloy and known for destabilizing the γ' precipitates [20, 27]. Suzuki et al. [20] showed Cr addition to Co–Al–W–Ta-based alloy results in earlier appearance of peak in yield strength versus temperature plot (at 1073 K) followed by rapid decrease. This observation was attributed to lower solvus temperature due to Cr addition. However, in the present case, we observe an increase in solvus temperature by 24 °C for 10Cr2Ta and 12 °C for 10Cr2Ta2Ti alloy compared to 2Ta and 2Ta2Ti, respectively. As mentioned in earlier section, this is mainly due to increase in Ta partitioning to γ' after Cr addition and thus also responsible for increase in stacking fault energy of γ' precipitates. Cr do have an effect on increasing the yield strength of some nickel-based superalloys (such as Hastelloy, Alloy 625) due to the formation of Ni₂ (Cr, Mo) precipitates after prolonged aging [63, 64]. Figure 5b shows a comparison of specific 0.2% proof stress values at 870 °C for 10Cr2Ta/10Cr2Ta2Ti alloys with 2Ta/2Ta2Ti alloys, Co–Al–W-based and nickel-based MAR-M-247 alloy. Due to higher density, Co–9Al–9.8W and Co–8.8Al–9.8W–2Ta alloys have lower values of 32.6 and 57.4 MPa/gm.cm⁻³, respectively. The present alloys, 10Cr2Ta and 10Cr2Ta2Ti, show 73.4 and 85.6 MPa/gm.cm⁻³, respectively, that are even higher than nickel-based superalloys.

Conclusions

The main conclusions from the present article are: Cr additions alter the cuboidal morphology of γ' precipitates in Co–30Ni–10Al–5Mo–2Ta and Co–30Ni–

10Al–5Mo–2Ta–2Ti, i.e., the precipitates tend to adopt spherical morphology.

With the addition of Cr, the Mo partitioning, i.e., K_{Mo} , becomes <1. Ab initio calculations indicate that the Cr prefers to replace Mo atoms of the L₁₂ unit cell, consequently altering the nature of partitioning of Mo ($K_{Mo} > 1$ to $K_{Mo} < 1$).

The solvus temperature of the 10Cr2Ta and 10Cr2Ta2Ti alloys was measured to be 1038 and 1078 °C, respectively. The measured densities of these Cr-containing alloys are in the range between 8.41 and 8.52 gm.cm⁻³ that is much lower than Co–Al–W-based alloys and comparable to typical nickel-based superalloys.

The 10Cr2Ta2Ti alloy exhibits a 0.2% proof stress of 720 MPa at 870 °C which is significantly higher than other Co–Al–W-based alloys and even nickel-based superalloys. In addition, due to their lower density, these alloys show higher specific strength.

Acknowledgements

Open access funding provided by Max Planck Society. All the authors would like to acknowledge the microscope facility available at Advanced Facility for Microscopy and Microanalysis (AFMM) center, Indian Institute of Science, Bangalore. The authors also thank the Supercomputer Education and Research Centre and Materials Research Centre, IISc, for providing the required computational facilities. One of the authors (KC) would like to thank ARDB GT Map programme for support. TA and RB would like to acknowledge the use of atom probe tomography facilities in the center for Advanced Research and Technology (CART) at University of North Texas (UNT).

Compliance with ethical standards

Conflict of interest The authors declare that they have no conflicts of interests.

Open Access This article is distributed under the terms of the Creative Commons Attribution 4.0 International License (<http://creativecommons.org/licenses/by/4.0/>), which permits unrestricted use, distribution, and reproduction in any medium, provided you give appropriate credit to the original author(s) and the source, provide a link to the

Creative Commons license, and indicate if changes were made.

References

- [1] Perepezko JH (2009) The hotter the engine, the better. *Science* 326:1068–1069
- [2] Pollock TM (2016) Alloy design for aircraft engines. *Nat Mater* 15:809–815
- [3] Reed RC, Tao T, Warnken N (2009) Alloys-by-design: application to nickel-based single crystal superalloys. *Acta Mater* 57:5898–5913
- [4] Antony KC (1983) Wear-resistant cobalt-base alloys. *JOM* 35:52–60
- [5] Riddihough M (1970) Stellite as a wear-resistant material. *Tribology* 3:211–215
- [6] Lee CS (1971) Precipitation-hardening characteristics of ternary Cobalt–Aluminium–X alloys. Ph.D. thesis, University of Arizona
- [7] Sato J, Omori T, Oikawa K et al (2006) Cobalt-base high-temperature alloys. *Science* 312:90–91
- [8] Pollock TM, Dibbern J, Tsunekane M et al (2010) New Co-based γ - γ' high-temperature alloys. *JOM* 62:58–63
- [9] Suzuki A, Inui H, Pollock TM (2015) L12-strengthened cobalt-base superalloys. *Annu Rev Mater Res* 45:345–368
- [10] Coutsouradis D, Davin A, Lamberigts M (1987) Cobalt-based superalloys for applications in gas turbines. *Mater Sci Eng* 88:11–19
- [11] Stringer J (1977) Hot corrosion of high-temperature alloys. *Annu Rev Mater Sci* 7:477–509
- [12] Di Martino J, Rapin C, Berthod P et al (2004) Corrosion of metals and alloys in molten glasses. Part 2: nickel and cobalt high chromium superalloys behaviour and protection. *Corros Sci* 46:1865–1881
- [13] Padture NP, Gell M, Jordan EH (2002) Thermal barrier coatings for gas-turbine engine applications. *Science* 296:280–284
- [14] Clarke DR, Oechsner M, Padture NP (2012) Thermal-barrier coatings for more efficient gas-turbine engines. *MRS Bull* 37:891–898
- [15] Klein L, Bauer A, Neumeier S et al (2011) High temperature oxidation of γ/γ' -strengthened Co-base superalloys. *Corros Sci* 53:2027–2034
- [16] Klein L, Shen Y, Killian MS, Virtanen S (2011) Effect of B and Cr on the high temperature oxidation behaviour of novel γ/γ' -strengthened Co-base superalloys. *Corros Sci* 53:2713–2720
- [17] Yan H-Y, Vorontsov VA, Dye D (2014) Effect of alloying on the oxidation behaviour of Co–Al–W superalloys. *Corros Sci* 83:382–395
- [18] Shinagawa K, Omori T, Oikawa K et al (2009) Ductility enhancement by boron addition in Co–Al–W high-temperature alloys. *Scr Mater* 61:612–615
- [19] Xue F, Zhou HJ, Shi QY et al (2015) Creep behavior in a γ' strengthened Co–Al–W–Ta–Ti single-crystal alloy at 1000 °C. *Scr Mater* 97:37–40
- [20] Suzuki A, Pollock TM (2008) High-temperature strength and deformation of γ/γ' two-phase Co–Al–W-base alloys. *Acta Mater* 56:1288–1297
- [21] Povstugar I, Choi P-P, Neumeier S et al (2014) Elemental partitioning and mechanical properties of Ti- and Ta-containing Co–Al–W-base superalloys studied by atom probe tomography and nanoindentation. *Acta Mater* 78:78–85
- [22] Tanaka K, Ooshima M, Tsuno N et al (2012) Creep deformation of single crystals of new Co–Al–W-based alloys with fcc/L12 two-phase microstructures. *Philos Mag* 92:4011–4027
- [23] Okamoto NL, Oohashi T, Adachi H et al (2011) Plastic deformation of polycrystals of Co₃(Al, W) with the L12 structure. *Philos Mag* 91:3667–3684
- [24] Meher S, Nag S, Tiley J et al (2013) Coarsening kinetics of γ' precipitates in cobalt-base alloys. *Acta Mater* 61:4266–4276
- [25] Vorontsov VA, Barnard JS, Rahman KM et al (2016) Coarsening behaviour and interfacial structure of γ' precipitates in Co–Al–W based superalloys. *Acta Mater* 120:14–23
- [26] Shinagawa K, Omori T, Sato J et al (2008) Phase equilibria and microstructure on γ' phase in Co–Ni–Al–W system. *Mater Trans* 49:1474–1479
- [27] Ooshima M, Tanaka K, Okamoto NL et al (2010) Effects of quaternary alloying elements on the γ' solvus temperature of Co–Al–W based alloys with fcc/L12 two-phase microstructures. *J Alloys Compd* 508:71–78
- [28] Yan H-Y, Coakley J, Vorontsov VA et al (2014) Alloying and the micromechanics of Co–Al–W–X quaternary alloys. *Mater Sci Eng A* 613:201–208
- [29] Knop M, Mulvey P, Ismail F et al (2014) A new polycrystalline Co–Ni superalloy. *JOM* 66:2495–2501
- [30] Neumeier S, Freund LP, Göken M (2015) Novel wrought γ/γ' cobalt base superalloys with high strength and improved oxidation resistance. *Scr Mater* 109:104–107
- [31] Zenk CH, Neumeier S, Engl NM et al (2016) Intermediate Co/Ni-base model superalloys—thermophysical properties, creep and oxidation. *Scr Mater* 112:83–86
- [32] Feng G, Li H, Li SS, Sha JB (2012) Effect of Mo additions on microstructure and tensile behavior of a Co–Al–W–Ta–B alloy at room temperature. *Scr Mater* 67:499–502
- [33] Pyczak F, Bauer A, Göken M et al (2015) The effect of tungsten content on the properties of L12-hardened Co–Al–W alloys. *J Alloys Compd* 632:110–115

- [34] Makineni SK, Nithin B, Chattopadhyay K (2015) A new tungsten-free γ - γ' Co–Al–Mo–Nb-based superalloy. *Scr Mater* 98:36–39
- [35] Makineni SK, Nithin B, Chattopadhyay K (2015) Synthesis of a new tungsten-free γ - γ' cobalt-based superalloy by tuning alloying additions. *Acta Mater* 85:85–94
- [36] Makineni SK, Samanta A, Rojhirunsakool T et al (2015) A new class of high strength high temperature cobalt based γ - γ' Co–Mo–Al alloys stabilized with Ta addition. *Acta Mater* 97:29–40
- [37] Makineni SK, Nithin B, Palanisamy D, Chattopadhyay K (2016) Phase evolution and crystallography of precipitates during decomposition of new “tungsten-free” Co(Ni)–Mo–Al–Nb γ - γ' superalloys at elevated temperatures. *J Mater Sci* 51:7843–7860. doi:10.1007/s10853-016-0026-1
- [38] Liu Q, Coakley J, Seidman DN, Dunand DC (2016) Precipitate evolution and creep behavior of a W-free Co-based superalloy. *Metall Mater Trans A* 47:1–7
- [39] Sharma A, Agrawal P, Pandey P et al (2016) High temperature creep of tungsten free cobalt based superalloys. Beyond nickel based superalloys II. http://dc.engconfintl.org/superalloys_ii/43
- [40] Caron P, Khan T (1999) Evolution of Ni-based superalloys for single crystal gas turbine blade applications. *Aerosp Sci Technol* 3:513–523
- [41] Caron P (2000) High γ ' solvus new generation nickel-based superalloys for single crystal turbine blade applications. *Superalloys 2000*:737–746
- [42] Povstugar I, Zenk CH, Li R et al (2016) Elemental partitioning, lattice misfit and creep behaviour of Cr containing γ' strengthened Co base superalloys. *Mater Sci Technol* 32:220–225
- [43] Kresse G, Furthmüller J (1996) Efficient iterative schemes for ab initio total-energy calculations using a plane-wave basis set. *Phys Rev B* 54:11169–11186
- [44] Kresse G, Furthmüller J (1996) Efficiency of ab initio total energy calculations for metals and semiconductors using a plane-wave basis set. *Comput Mater Sci* 6:15–50
- [45] Kresse G, Joubert D (1999) From ultrasoft pseudopotentials to the projector augmented-wave method. *Phys Rev B* 59:1758–1775
- [46] Perdew JP, Burke K, Ernzerhof M (1996) Generalized gradient approximation made simple. *Phys Rev Lett* 77:3865–3868
- [47] Monkhorst HJ, Pack JD (1976) Special points for Brillouin-zone integrations. *Phys Rev B* 13:5188–5192
- [48] Stevanović V, Lany S, Zhang X, Zunger A (2012) Correcting density functional theory for accurate predictions of compound enthalpies of formation: fitted elemental-phase reference energies. *Phys Rev B* 85:115104
- [49] Mughrabi H (2014) The importance of sign and magnitude of γ/γ' lattice misfit in superalloys—with special reference to the new γ' -hardened cobalt-base superalloys. *Acta Mater* 81:21–29
- [50] Meher S, Carroll LJ, Pollock TM, Carroll MC (2016) Solute partitioning in multi-component γ/γ' Co–Ni-base superalloys with near-zero lattice misfit. *Scr Mater* 113:185–189
- [51] Yoon KE, Isheim D, Noebe RD, Seidman DN (2001) Nanoscale studies of the chemistry of a René N6 superalloy. *Interface Sci* 9:249–255
- [52] Huang M, Cheng Z, Xiong J et al (2014) Coupling between Re segregation and γ/γ' interfacial dislocations during high-temperature, low-stress creep of a nickel-based single-crystal superalloy. *Acta Mater* 76:294–305
- [53] Amouyal Y, Mao Z, Seidman DN (2008) Segregation of tungsten at $\gamma'(L12)/\gamma(\text{fcc})$ interfaces in a Ni-based superalloy: an atom-probe tomographic and first-principles study. *Appl Phys Lett* 93:201905
- [54] Booth-Morrison C, Weninger J, Sudbrack CK et al (2008) Effects of solute concentrations on kinetic pathways in Ni–Al–Cr alloys. *Acta Mater* 56:3422–3438
- [55] Booth-Morrison C, Noebe RD, Seidman DN (2009) Effects of tantalum on the temporal evolution of a model Ni–Al–Cr superalloy during phase decomposition. *Acta Mater* 57:909–920
- [56] Davis JR, Allen P, Lampman S et al (1990) *Metals handbook*. Vol 1. Properties and selection: iron, steels, and high-performance alloys, 10th edn. ASM International, Materials Park, OH, pp 2322–2325
- [57] Hong YM, Mishima Y, Suzuki T (1988) Accurate determination of γ' solvus in Ni–Al–X ternary systems. *MRS Online Proc Libr Arch*. doi:10.1557/PROC133429
- [58] Baldan R, Nunes CA, Barboza MJR et al (2009) Tensile properties of MAR-M-247 superalloy. In: *Int. Conf. Adv. Mater. SBPMat*, vol 11
- [59] Suzuki A, DeNolf GC, Pollock TM (2007) Flow stress anomalies in γ/γ' two-phase Co–Al–W-base alloys. *Scr Mater* 56:385–388
- [60] Hirsch PB (1992) A model of the anomalous yield stress for (111) slip in L1 2 alloys. *Prog Mater Sci* 36:63–88
- [61] Paidar V, Pope DP, Vitek V (1984) A theory of the anomalous yield behavior in L12 ordered alloys. *Acta Metall* 32:435–448
- [62] Mottura A, Janotti A, Pollock TM (2012) A first-principles study of the effect of Ta on the superlattice intrinsic stacking fault energy of L12-Co3(Al, W). *Intermetallics* 28:138–143
- [63] Sundararaman M, Kumar L, Prasad GE et al (1999) Precipitation of an intermetallic phase with Pt2Mo-type structure in alloy 625. *Metall Mater Trans A* 30:41–52
- [64] Tawancy HM (1980) Order-strengthening in a nickel-base superalloy (hastelloy alloy S). *Metall Trans A* 11:1764–1765